

Finite Element Simulation of a Protein Analysis Nanopore

Abstract

The goal of this simulation effort was to better understand the potential for biomolecule analysis of an inverted pyramidal silicon nanopore structure. The geometry was chosen in part because etching allows small pore exit dimensions with length tolerances controlled by the surface etch mask. Epitaxial growth enables well-defined field effect transistor (FET) axial dimensions. The system studied has FETs embedded in the pore walls as detectors and uses electro-osmosis force (EOF) to move biomolecules past them. Since the biomolecules of initial interest are proteins in the kDa mass range, a continuum representation of the fluid with the biomolecules modeled as hard spheres with a net charge was used. The finite element simultaneous solution of the Poisson Nernst-Plank ion transport and Navier-Stokes fluid flow equations is achieved by alternating between iterative Newton solutions until quantities common to both sets of equations are consistent¹. In contrast with pores with parallel channel walls, for relatively large potential differences across the pore region, the resulting steady flow solution has a stable vortex close to the entrance due to back pressure caused by the narrowed exit. The flow then exiting the pore is concentrated in a narrow region along the pore walls in the wider part of the pore and nearly uniform across the pore only close to the exit. The flow is upwards just above the entrance centered near the axis. Biomolecules of both charges, captured from a narrow region just above the pore edges, are moved close to the pore walls, and thus the detectors, by the EOF push. This force dominates the electrical force for realistic biomolecule net charges enhancing detector charge and spatial resolution compared to the geometries of pores with parallel walls.

Introduction

It has been proposed² that nanopores with embedded instrumentation might be used to analyze single biomolecules. The pioneers in the field of nanopore development for such analysis are Kasianowicz et al.³ and there were rapid developments shortly thereafter^{4,5,6}. This simulation was done in support of a project⁷ to study such a silicon-based system that had an inverted pyramidal pore with FET structures in the pore walls. The pore was formed by wet anisotropic etching of the {100} crystal plane with KOH thus forming an inverted pyramid. The pore exit has nanopore dimensions controlled by the surface etch mask with micron dimensions, the SOI active layer thickness, and the etch rate. The etching was done through epitaxially-grown vertical FETs with well-controlled doped regions. This construction scenario uses, by current standards, less than state-of-the-art techniques and relatively common silicon fabrication facilities. Molecules in an electrolyte are moved through the pore channel by the electro-osmosis force. Biomolecule analysis is performed as the variations in the charge structure of molecules passing near the FET gate regions cause detectable variations in FET source-drain current, that, with sufficient resolution, can be used to characterize the passing molecule.

Since the biomolecules are much larger and more massive than the electrolyte ions or water molecules, a continuum formulation should adequately represent their environment for motion at the time scales of interest. The appropriate equations are the Poisson-Nernst-Planck ion transport and Navier-Stokes fluid flow non-linear equations coupled through the common electrostatic potential and fluid velocity. Adaptive finite element numerical solutions can be used for the very rapid spatial potential variations in the fluid near the charged fluid/solid interface for the micron scale, relatively complex geometry of interest. It is near this interface where most of the crucial phenomena take place so the numerical solution should be able to handle distance scales from a few nanometers to several microns.

First a consistent fluid flow and electric field is found numerically solving the relevant equations. For low densities of analyzed molecules, their charge structure negligibly affects the surrounding field at distances greater than a Debye length or two. In this case, molecule trajectories can be found by integrating the force equation using the electric field and Stokes fluid drag as the relevant forces using the mass and net charge.

The choice for the finite element infrastructure was FreeFem++⁸, a system developed by Prof. Frédéric Hecht and his group at the Université Pierre and Marie Curie in Paris, France. In addition to being free and open source, it is well-supported with a high-level programming language that is a C++ idiom. It is also easily installed, has at least hundreds of active users, and runs on essentially all platforms. The code described here will be available on GitHub⁹ for readers that want to verify the results, better understand the physics, or adapt the code to a different microfluidic sensor configuration.

Equations Solved

The Poisson-Nernst-Planck equations describing the electrolyte ion transport¹⁰ are:

$$1) \quad \frac{\partial n_{\pm}}{\partial t} + \vec{\nabla} \cdot (n_{\pm} \vec{v}_{\pm}) = 0$$

$$\vec{v}_{\pm} = \pm b_{\pm} e \vec{E} - D_{\pm} \log(n_{\pm}) + \vec{u}$$

which is the mass continuity equation without sources or sinks for the positive and negative ions with density n_{\pm} and velocity \vec{v}_{\pm} . The mobility b_{\pm} is related to the dispersion coefficient by the Einstein relation $D_{\pm} = k_B T b_{\pm}$ with k_B the Boltzmann constant and T the Kelvin temperature. The three components of ion velocity are due to the electric field, dispersion from concentration gradient, and the bulk fluid velocity. The measured ion mobilities are nearly equal, so for convenience we will slightly simplify the equations by using their average mobility. The electric field is the negative gradient of the electrostatic potential $\vec{E} = -\vec{\nabla}\varphi$ and is related to the charge densities by Poisson's Equation

$$2) \quad -\vec{\nabla} \cdot \epsilon \vec{\nabla} \varphi = \rho$$

with ρ the charge density and ϵ the permittivity. This charge density is $(n_+ - n_-) e$ in the fluid but is the surface charge density σ at the fluid/solid interface. Equations 1) and 2) collectively are the Poisson-Nernst-Planck (PNP) equations.

The fluid velocity \vec{u} is coupled to the ion densities and electrostatic potential through the Navier-Stokes (N-S) equation with the body force the electric field times the charge density:

$$3) \quad \frac{\partial \vec{u}}{\partial t} + (\vec{u} \cdot \vec{\nabla}) \vec{u} + \frac{\vec{\nabla} P}{\rho_f} - \frac{\eta}{\rho_f} \Delta \vec{u} + \frac{\rho}{\rho_f} \vec{\nabla} \varphi = 0$$

where P is the pressure, η the dynamic viscosity, and ρ_f the fluid density. To facilitate numerical solution, these equations are put in non-dimensional form using characteristic values. Generally following Squires and Bazant⁹, the characteristic value scales are set by the magnitude of the external electric field E_0 , the

length scale in the pore region L_0 , and the bulk ion density in the electrolyte n_0 . Close to the fluid/solid interface, the length scale of the exponentially-falling potential is the Debye length,

$$\lambda_D = \sqrt{\frac{\epsilon_f k_B T}{2n_0 e^2}}$$

for a 1:1 electrolyte like KCl for a fluid with permittivity ϵ_f . The ratio $\delta = \lambda_d/L_0$ then connects these two length scales and is a small number as the Debye length is below 20 nm and the geometry length scale a micron or larger in most microfluidic applications. Another ratio connecting different scales is $\gamma = \epsilon_s/\epsilon_f$. This is the ratio of the permittivity of the solid forming the pore to that of the fluid in the pore, also less than 1 due to the large dielectric constant of water. To achieve the transformation of the equations to a form better suited to numerical solution, introduce:

$$\begin{aligned}\vec{x} &= L_0 \vec{x}^* \\ \vec{\nabla} &= \frac{1}{L_0} \vec{\nabla}^* \\ \vec{\nabla} \cdot \vec{\nabla} &= \Delta = \frac{1}{L_0^2} \Delta^* \\ \varphi_0 &= |\zeta| \\ U_0 &= bE_0/\varphi_0 \\ \psi &= e\varphi_0/k_B T \\ n_+ &= 2n_0 \psi n_+^* \\ n_- &= 2n_0 \psi n_-^* \\ \sigma &= \sigma_0 \sigma^* \\ \sigma_0 &= \sigma / 2n_0 e \psi L_0^2 \\ Pe &= U_0 L_0 / D \\ Re &= \rho_f U_0 L_0 / \eta\end{aligned}$$

The zero subscript indicates a characteristic value and the asterisk superscript a unitless variable whose magnitude is scaled by a characteristic value so it will not become too much greater than one for numerical solutions. The last two variables are the Péclet and Reynolds numbers respectively and the zeta potential is ζ .

The PNP equations then become:

$$4) \quad \begin{aligned}\frac{\partial p}{\partial t} - \psi \vec{\nabla} \cdot (p \vec{\nabla} \varphi) - \Delta p + (Pe) \vec{\nabla} \cdot (p \vec{u}) &= 0 \\ \frac{\partial n}{\partial t} + \psi \vec{\nabla} \cdot (n \vec{\nabla} \varphi) - \Delta n + (Pe) \vec{\nabla} \cdot (n \vec{u}) &= 0 \\ -\delta^2 \gamma \Delta \varphi &= (p - n) + \sigma_0 \sigma\end{aligned}$$

where the fluid velocity \vec{u} is scaled by U_0 and the electrostatic potential by φ_0 . In this equation the asterisk superscripts have been dropped and $p = n_+^*$ and $n = n_-^*$. The electrostatic potential φ (first term last equation) is in the entire domain with $\gamma = 1$ in the fluid and about 0.05 in the silicon dioxide insulator at the fluid/solid interface and 0.15 in the silicon membrane. The ion densities are only non-zero only in the fluid in the first term on the right-hand side in this equation. The last term containing the surface charge density σ is present on the charged surface of the fluid/solid interface. Note that these same equations, with the velocity of the medium $\vec{u} = 0$ and with the addition of sources and sinks, are the

core of the semiconductor drift-diffusion equations with much different boundary conditions and coefficients. This makes solving simultaneously for the FET behavior with the same underlying numerical techniques feasible although not done here.

Similarly scaling the N-S equation yields:

$$5) \quad \frac{\partial \vec{u}}{\partial t} + (Pe)(\vec{u} \cdot \vec{\nabla}) \vec{u} + \vec{\nabla}P - \frac{(Pe)}{(Re)} \Delta \vec{u} + \frac{e\phi_0 2n_0}{P_0} \psi(p - n) \vec{\nabla} \varphi = 0$$

where the pressure has been scaled by $P_0 = D\rho_f U_0 / L_0$. This is a vector equation made non-linear by the second and last terms and strongly coupled to the PNP equations which contain all the same unknowns except the pressure. Ascertaining appropriate initial and boundary conditions is crucial to obtaining meaningful results and is a non-trivial task.

Code Development and Description

The computational domain is an axisymmetric inverted cone instead of a 3D inverted pyramid chosen to decrease the computational cost without unduly compromising the physics results. Mesh density needs to be considerably higher near the fluid/solid interface since the phenomena of interest are controlled by the electrostatic potential there, set by the surface charge density, which falls off exponentially with distance from the interface. The Debye length, the distance scale of the exponential, is typically 10 nm or less whereas the features of the pore are in the micron range. The y-axis is the rotation axis with and the other borders are far enough from the pore region so that the relevant quantities (fluid flow and electric field) vary slowly. The angle of the cone wall to the horizontal, $\tan^{-1}(\sqrt{2}) = 54.7^\circ$ is set by the crystal structure of silicon and the much higher etch rate of the {100} silicon surface plane.

Since both sets of equations are non-linear and will be solved with an iterative Newton technique, the starting values for the electric field and fluid velocity should be close enough to the final solution to allow convergence. Physics considerations permit suitable initial values to be obtained.

Initial Potential and Fluid Velocity

The electric field, found as the negative gradient of the electrostatic potential $\vec{E} = -\vec{\nabla}\varphi$, determines the charge-dependent electrophoretic force, and through this same force on the movable outer counter-ions near the charged interface, the fluid flow from electro-osmosis. The initial potential is found solving Poisson's Equation with appropriate boundary conditions. The considerable surface charge due to the dissociation of silanol groups at the SiO₂ insulator is completely screened by the mobile electrolyte ions except within a few Debye lengths of the solid/fluid interface. Then an appropriate approximate potential to start the Newton iterations is found using only the potential difference at the domain top and bottom to impose an external electric field of magnitude $E_0 = 10 \text{ V/mm}$ and the permittivities of the fluid and solid regions. The choice of E_0 sets the potential difference across the domain height H as $\Delta V = E_0 H$.

An approximate initial flow is found by solving the Navier-Stokes equation with Oseen's added linear inertia term¹¹. The relevant boundary condition is forcing the flow velocity at the interface to equal the Helmholtz-Smoluchowski value. This value is $u_{interface} = -E_0 \epsilon \zeta / \eta$ where ϵ is the fluid permittivity, ζ is the zeta potential at the shear plane, and η is the fluid's dynamic viscosity. The zeta potential, which characterizes the electrical double layer at the interface, is experimentally measured in geometries for which the Helmholtz-Smoluchowski equation is valid. It is an indirect measure of the underlying surface

charge density at the interface which is very difficult to measure directly. It has the experimental value of about -100 mV at the pH and temperature of the simulated configuration¹².

The initial potential and fluid velocity thus found are shown in Figure 1 for both a well-studied cylindrical geometry used as a check on the numerical approach and the inverted cone geometry studied here. Figures 1a and 1b depict the initial potential in the pore region for the cylindrical and inverted cone geometries respectively. Figures 1c and 1d show the scaled initial fluid flow velocity for the same geometries with Fig. 1d also showing the pressure isolines. The minimum radius given sets the scale. In Figure 1c, the expected plug flow is clearly visible. In Figure 1d, the upper region away from the pore wall exhibits a vortex due to the back pressure from the narrowed exit. This results in an upward flow, weaker than the strong downward flow in a narrow region near the pore wall, over much of the upper portion of the pore. As seen later, the final fluid velocity found is quite similar to that shown here, but the solution potential is altered to have almost all the variation in the pore fluid region and the pore membrane. Nevertheless, this potential is simple to obtain and good enough to allow an iterative solution.

The flow diagram for the computational ansatz is shown in Figure 2. After initialization of a guessed flow and potential, the computation proceeds by alternating between two Newton iterations. First, for fixed potential and ion densities, the Navier-Stokes equation is solved with the last term in 5) initially zero as $n = p = n_0$. For the next Newton solve for the electrostatic potential and ion densities, modeling the fluid/solid interface requires some care. Simply using the zeta potential at this surface fails to accurately represent the potential and its shape in this geometry with corners at the micron scale. The zeta potential represents the potential at the slip plane separating mobile from bound counter ions due to partial screening of the surface charge over a surface area more than a micron in extent. Thus a more accurate representation of the potential in the first few Debye lengths away from the surface should be based more directly on the surface charge density which is less affected by micron-scale geometric changes. This is found by mimicking the basic features of the configuration for which the zeta potential is measured, finding the enclosed net charge using Gauss' Law, and using this to compute an equivalent surface charge density. This configuration is a plane of infinite extent with a surface zeta potential -100 mV . The surface charge density thus found is $-6.91 * 10^{-12} \text{ C/m}^2$.

Figure 3 contrasts the scaled electric field at the bottom of a conical pore of exit radius 0.2 micron and depth 2 microns using a constant zeta potential (Fig. 3a) and a constant equivalent surface charge (Fig. 3b). The external electric field would be 10 V/mm in this cylindrical geometry if not altered by the presence of the pore membrane. Both the shape and the magnitude of the electric field differ significantly. Note the factor of 4 scale change in vector magnitude and the change in direction at the pore exit.

In the first stage of the main compute loop, the scaled Navier-Stokes equations 5) are solved using the Oseen algorithm by Newton iteration at fixed ion densities (p, n) and electrostatic potential φ . The scaled variational of the function (F) form in the Newton iteration (DF-F where DF is the differential with respect to the unknowns) is¹³

$$6) \quad \begin{aligned} & \frac{(Pe)}{(Re)} \int_{\Omega_f} (\vec{\nabla} \vec{u} : \vec{\nabla} \vec{v}) r d\omega + \frac{(Pe)}{(Re)} \int_{\Omega_f} u_r v_r \frac{1}{r} d\omega + (Pe) \int_{\Omega_f} (\vec{u} \cdot \vec{\nabla}) \vec{u} \cdot \vec{v} r d\omega \\ & - \int_{\Omega_f} (\vec{\nabla} \cdot \vec{v}) P r d\omega - \int_{\Omega_f} v_r P d\omega - \int_{\Omega_f} (\vec{f} \cdot \vec{v}) r d\omega \\ & - \int_{\Omega_f} (\vec{\nabla} \cdot \vec{u}) Q r d\omega - \int_{\Omega_f} u_r Q d\omega . \end{aligned}$$

Here the test function, a vector, paired with \vec{u} is \vec{v} , and the scalar paired with the pressure P is Q . The variables have been scaled with their characteristic values very similarly to the pioneering paper by Squires and Bazant⁹. The region Ω_f is the fluid portion of the computational domain with differential $d\omega = dr dz$. The characteristic pressure used is $P_0 = D\rho_f U_0 / L_0$ and the scaled electrostatic force is:

$$\vec{f} = \frac{e \varphi_0 2n_0 \psi (p - n)}{P_0} \vec{\nabla} \varphi$$

The first time through the loop this term is zero as the ion densities p and n are equal for the guessed initial state. On subsequent passes, the densities and the electrostatic potential use the values from the Poisson-Nernst-Planck solution second stage at that iteration. The operations on vectors using $\vec{\nabla}$ may be equivalently expressed using the Einstein summation convention as:

$$\begin{aligned} \vec{\nabla} \vec{u} : \vec{\nabla} \vec{v} &= \partial_i u_j \partial_i v_j \\ (\vec{u} \cdot \vec{\nabla}) \vec{u} \cdot \vec{v} &= (u_i \partial_i u_j) v_j \end{aligned}$$

Main loop, Poisson-Nernst-Planck second stage

The variational F form of the scaled, axisymmetric Poisson-Nernst-Planck equations 4) is:

$$\begin{aligned} &\int_{\Omega_f} (\vec{\nabla} p \cdot \vec{\nabla} q + \psi p \vec{\nabla} \phi \cdot \vec{\nabla} q - (\text{Pe}) p \vec{u} \cdot \vec{\nabla} q) r d\omega \\ &+ \int_{\Omega_f} (\vec{\nabla} n \cdot \vec{\nabla} m - \psi n \vec{\nabla} \phi \cdot \vec{\nabla} m - (\text{Pe}) n \vec{u} \cdot \vec{\nabla} m) r d\omega \\ &+ \int_{\Omega_s} (\delta^2 \psi \vec{\nabla} \phi \cdot \vec{\nabla} \chi - (p - n) \chi) r d\omega \\ &+ \int_{\Omega_s} (\delta^2 \psi \gamma \vec{\nabla} \phi \cdot \vec{\nabla} \chi) r d\omega \end{aligned}$$

Here q is the test function paired with the position ion number density p , m with the negative density n , and χ with the electrostatic potential ϕ . The Newton iteration based on this form finds new densities and electrostatic potential at this iteration of the mail loop with the fluid velocity fixed from the prior N-S stage. The region Ω_s is that of the solid in the entire computational domain.

At the end of each iteration in the main computational loop, the sum of the difference between the current and prior values of the ion densities, electrostatic potential, and fluid velocity is used as the measure of convergence. When this is negligible, the iteration is terminated.

In the simplest geometry, a plane, in the Debye-Hückel small surface charge limit, the net charge density $(n_+ - n_-) e$ is a decaying exponential analytically. For a few micron radius cylinder with a several micron depth, approximating the simple configuration close to the surface, the computation above reproduces this exponential decay as shown in Fig. 4 showing the logarithm of the net charge density drops linearly by nearly 6 orders of magnitude in the first 10 Debye lengths out from the slip plane.

Protein trajectories

Equating the net force on a sphere of mass m and net charge q in a fluid moving with velocity v_r relative to the fluid to the difference between the electrical force and the drag force resisting motion yields the drag equation

$$m \frac{dv_r}{dt} = qE - \frac{1}{2} \rho_f v_r^2 A C_d$$

assuming the charged sphere doesn't significantly perturb the electric field magnitude E or the fluid velocity. The fluid density is ρ_f , A is the sphere's cross section area, and C_d is the drag coefficient. This Riccati equation can be solved¹⁴ to yield

$$t = (1/\alpha g) \tanh^{-1}(\alpha v_r) \text{ or equivalently } v_r = (1/\alpha) \tanh(\alpha g t).$$

where $\alpha = (\rho_f A C_d / 2qE)$ and $g = qE/m$. Since the limit of $\tanh(x) = 1$ as $x \rightarrow \infty$, the terminal velocity of the sphere relative to the fluid velocity is $v_t = 1/\alpha$. Proteins are modeled as charged hard spheres with a radius, using the protein's mass m_p and density $\rho_p = 1.37 \text{ g/cm}^3$ given by¹⁵ $r_p = (3m_p / 4\pi\rho_p)^{1/3}$ which is $r_p = 0.66 m_p^{1/3}$ for radius in nm and mass in kDa. This nanometer-scale radius means the Reynolds number $Re = \rho_f 2r v_t / \eta$ is much less than 1 so the drag coefficient is $24/Re^{16}$ for a wide range of values of the parameters accessible in the laboratory. Then, at low Reynolds number, the drag force term is proportional to v_r and becomes $-6\pi\eta r_p v_r$. The time required to reach 1/2 of the terminal velocity, $v_t = qE / 6\pi r_p \eta$, is then at the picosecond scale, $t_{1/2} = (m_p / 6\pi\eta r_p) \tanh^{-1}(1/2)$, much shorter than the milli- or micro-second scale of laboratory observations of particle movement. Coupled with the relatively slow variation of \vec{E} and \vec{u} at the sub-micron scale, numerical integration of the drag equation over laboratory distances can then be split into two phases. In the first, with a time increment a fraction of $t_{1/2}$ and lasting until the particle velocity is very close to the terminal velocity, the particle hardly moves at all. Then, in the second phase, with the time increment much larger, the particle is advanced using the phase 1 relative velocity, \vec{E} , and \vec{u} until the difference between the phase 1 velocity and the current terminal velocity is greater than 1% or so. Then the phase 1 code is re-entered, re-establishing an appropriate drift velocity, and the phases alternated in this fashion until a preset position is reached.

As a check on the code, representative trajectories are calculated for 150 kDa proteins originating above a cylindrical pore of 2 microns in radius and 8 microns depth for a typical electric field of 10 V/mm.¹⁰ From the literature and experimental results, it is expected that the EOF velocity field in the pore is nearly uniform, if somewhat larger at the pore walls, and that protein trajectories would follow the fluid flow having approximately uniform density within the pore. As seen in Fig. 5, these expectations are met. Fig. 5a is the electric field, Fig. 5b the fluid velocity, and Fig. 5c three representative orbits for these parameters. In Figs. 5a and 5b, the individual vector arrows aren't visible as the underlying mesh points are too close together, but the color denotes the magnitude. In this and subsequent figures, the variables are scaled.

However, in the case of a pore in the shape of an inverted cone as in Fig. 6 with the same potential difference across the domain, the electric field, which is inversely proportional to the area, is concentrated near the pore exit. The resulting fluid flow driven by the field moving the mobile positive ions near the pore walls, is shown in Fig. 6a. The flow velocity increases towards and below the exit opening. In addition, because of the back pressure of the fluid trying to exit in a narrowing channel, a weak vortex develops near the pore axis. This

vortex pushes exiting particles closer to the wall. Some orbits that start closer to the axis are in the region where the flow is upwards and do not exit the pore. Representative orbits of those particles that exit the pore are shown in Fig. 6b. The cone has an exit radius of 200 nm, a depth of 2 microns, and the silicon V-groove opening angle of 54.7°. The net charge of the particles here is -25 e, larger than the negative net charge of any protein in an electrolyte, indicating that, because of the large drag force relative to the electrical force, nearly all captured particles starting from above the pore will be driven downwards with the EOF flow.

Doubling the potential to give an external field of 20 V/mm across a uniform domain results in the fluid velocity field as in Fig. 7a. Note the scale changes and that the vortex near the axis a little above the pore exit is much more prominent. The captured particles are now compressed into a narrow spatial band near the pore wall, as seen in Fig. 7b, with only those entering nearest the pore top outer edge exiting the pore.

Conclusions

These results indicate that, with easily achievable fabrication and operating parameters, nanopore configurations are attainable that force EOF-driven particles with arbitrary net charge traversing an inverted cone structure to travel in a narrow spatial band near the pore walls. This is the result of the shape of the electric and the fluid flow fields, the later heavily influenced by the back pressure caused by the downstream narrowing region. For example, an inverted pyramidal pore formed by KOH etching of silicon, with the electric field established by a few volt difference across a few micron membrane, is such a configuration. This property may be useful to enhance the capability of detectors embedded in the pore walls. Then regardless of charge, all captured particles from above the pore will move in similar paths close to the pore wall with a velocity proportional to their effective radius and the external applied field.

Figures

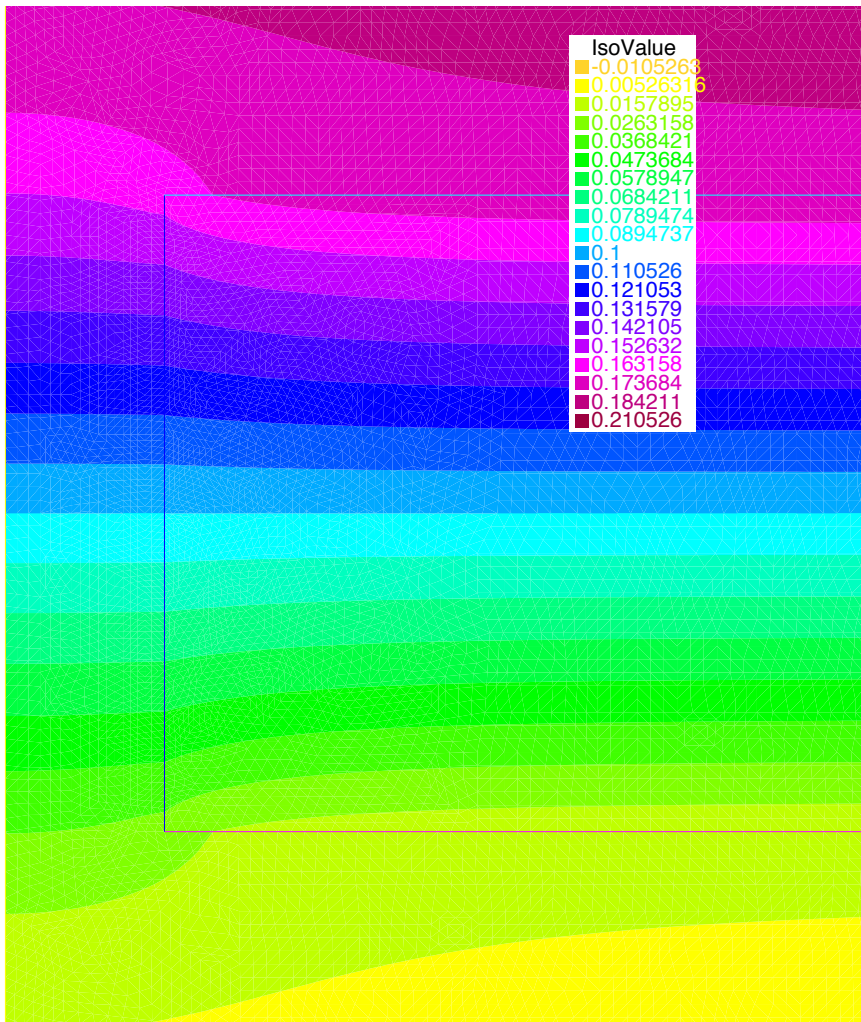


Fig. 1a – Electrostatic potential for axisymmetric cylinder,
radius = 2 microns, depth = 8 microns, external field = 10 V/mm.

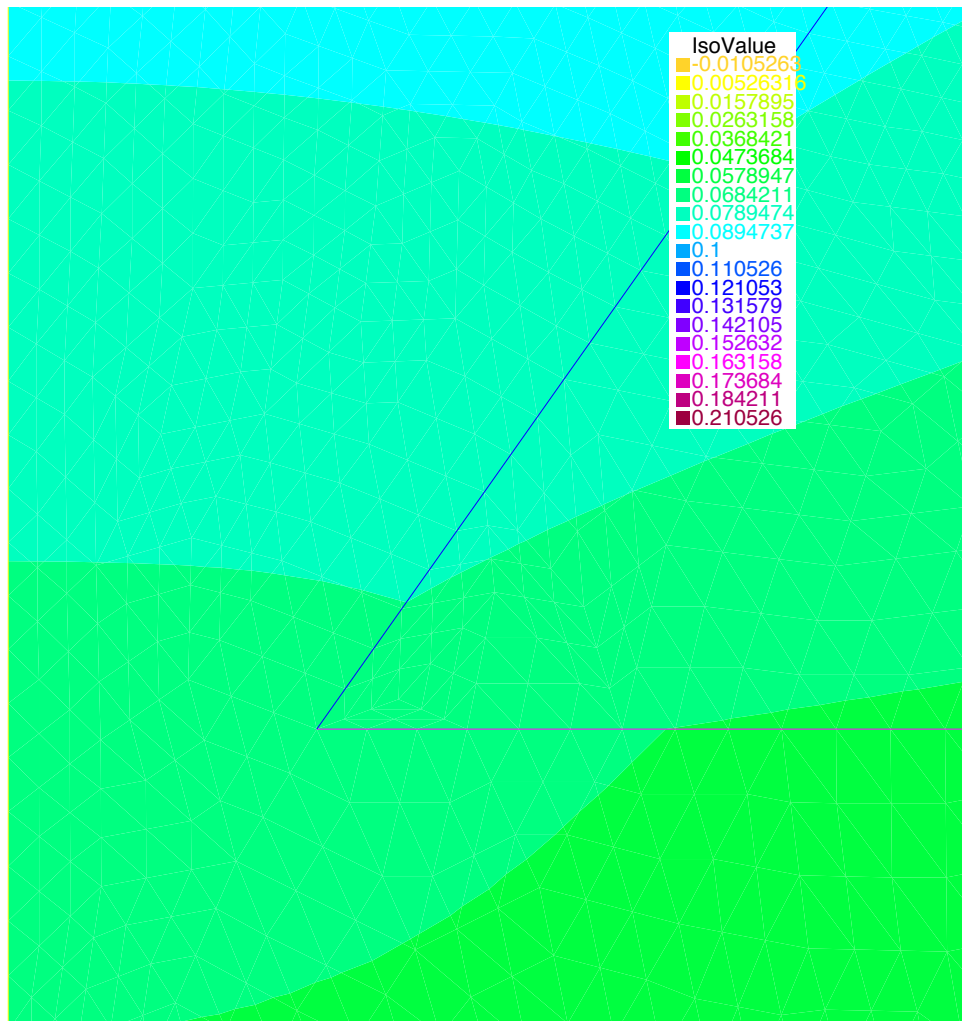


Fig. 1b – Electrostatic potential for inverted cone, min. radius = 100 nm, depth = 2 microns, external field = 10 V/mm.

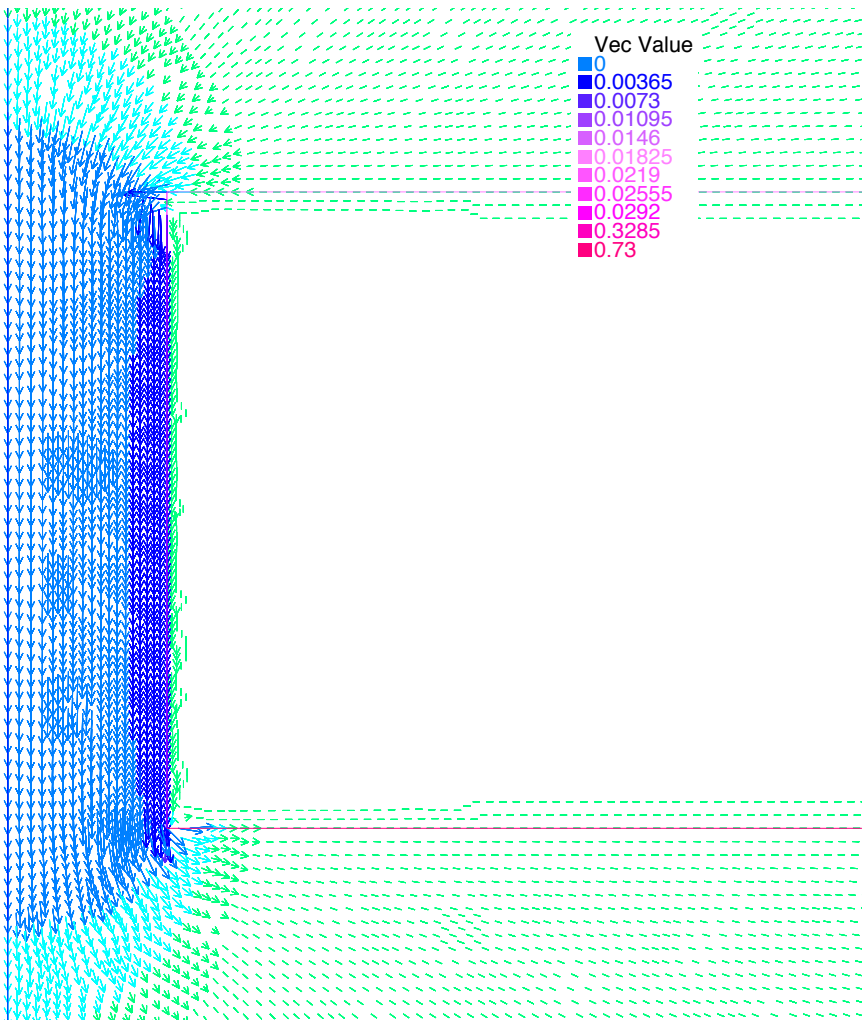


Fig. 1c – Scaled fluid velocity, same configuration as Fig. 1a.

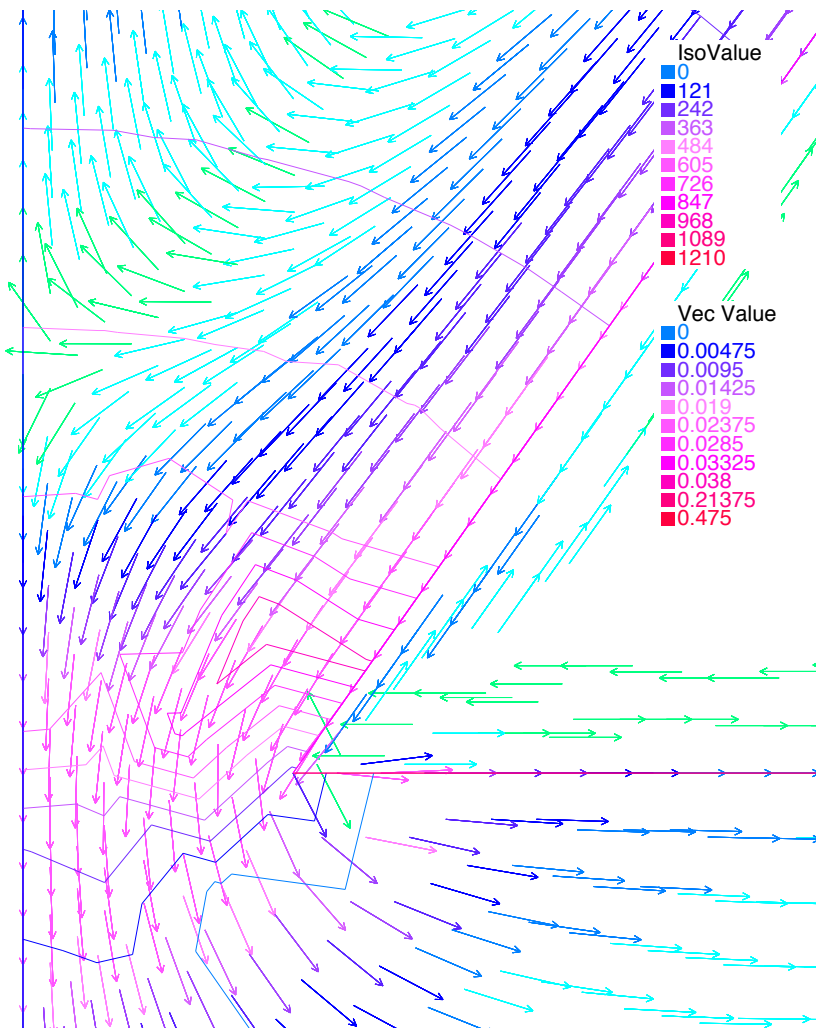


Fig. 1d – Scaled fluid velocity, same configuration as Fig. 1b.

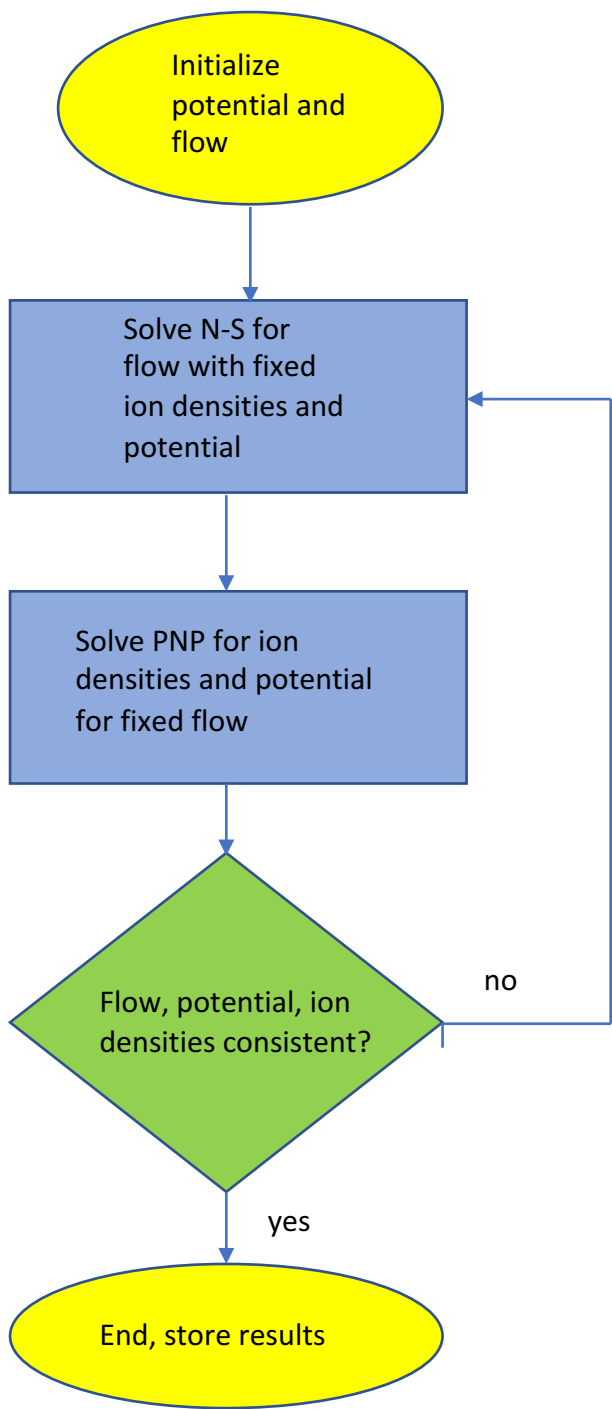


Fig. 2 – Computational flow diagram.

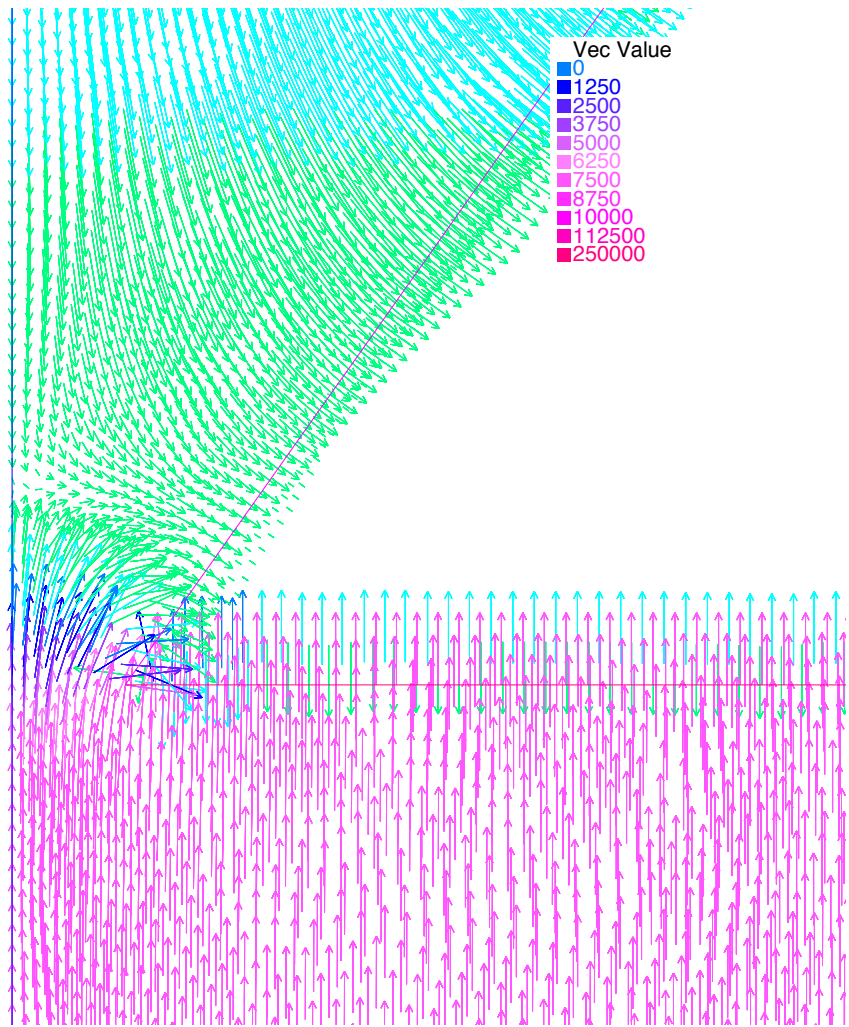


Fig. 3a – Electric field for inverted cone, minimum radius 0.2 micron, depth 2 microns, constant zeta potential, 10 V/mm external field.

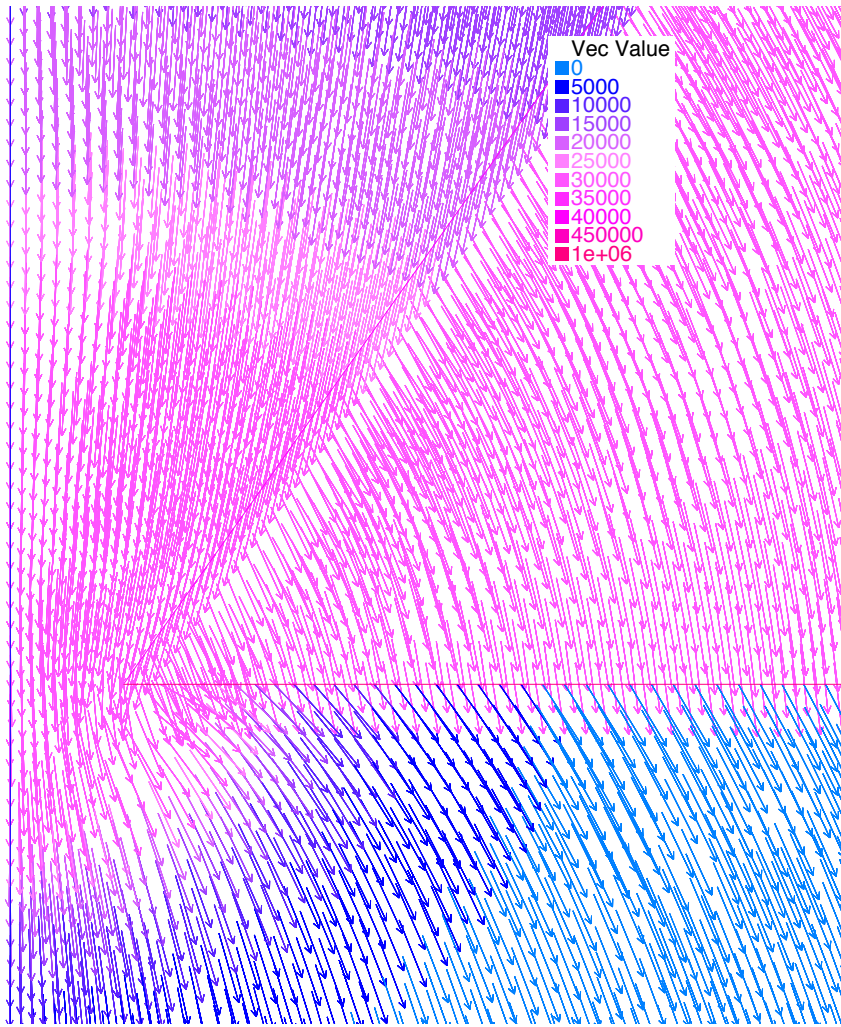


Fig. 3b – Electric field, same geometry as Fig. 3a except constant surface charge equivalent to the constant zeta potential. Note factor of 4 scale change and field direction in the pore.

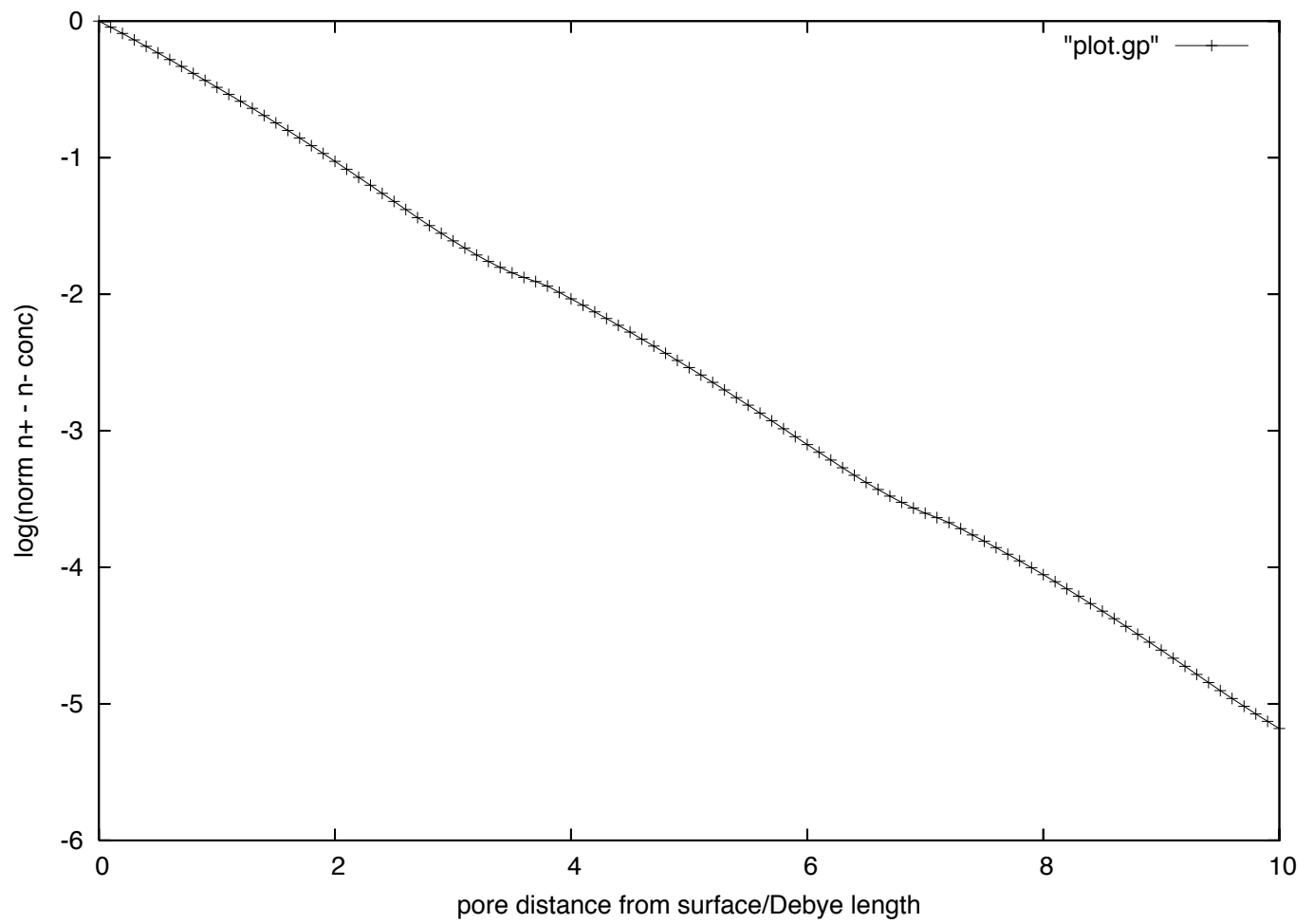


Fig. 4 – Log of the electrolyte net charge density close to the interface surface slip plane

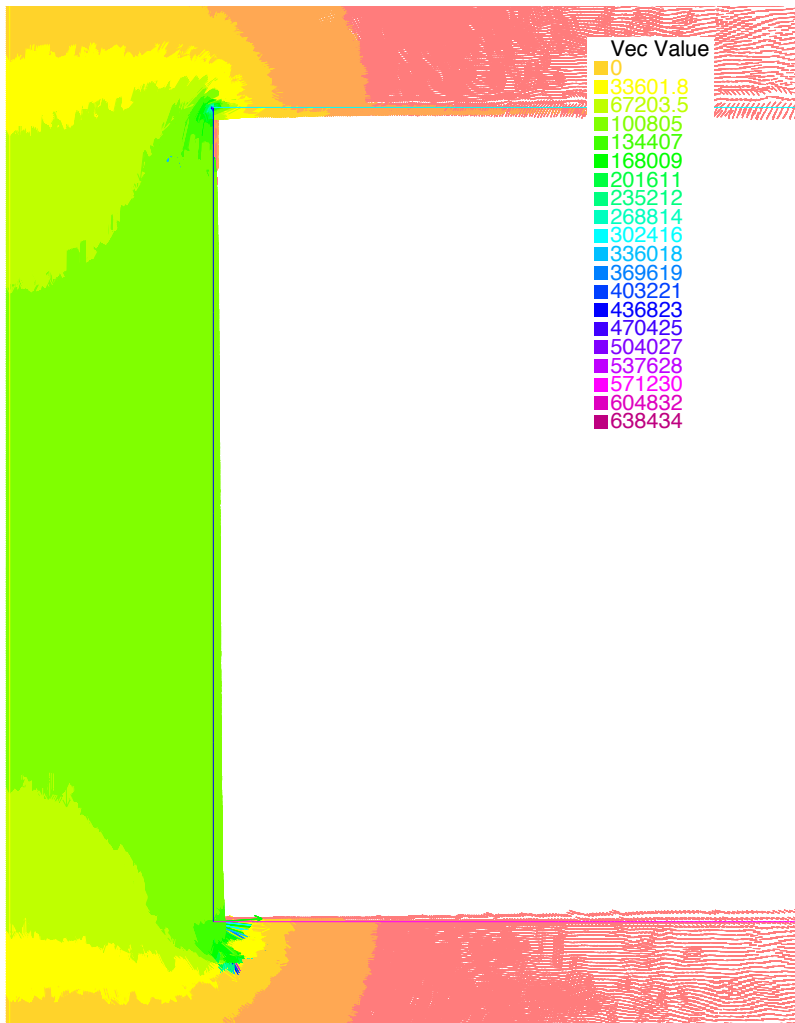


Fig. 5a – Scaled electric field for cylinder (radius 2 microns, depth 8 microns, external field 10 V/mm).

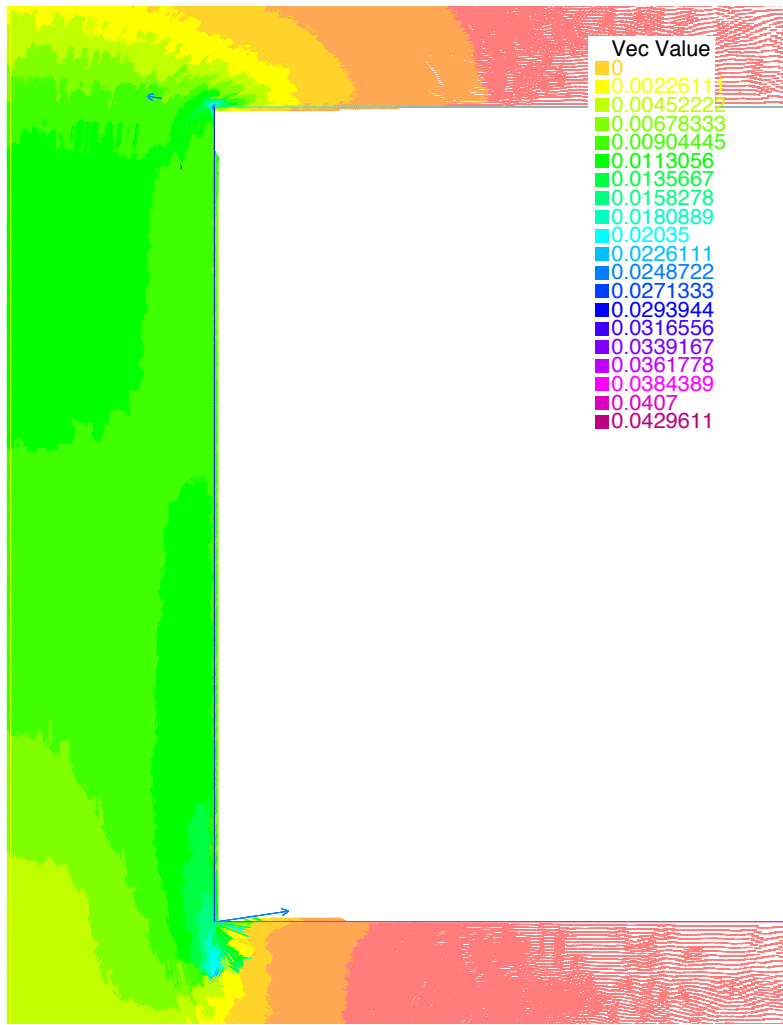


Fig. 5a – Scaled fluid velocity for cylinder (radius 2 microns, depth 8 microns, external field 10 V/mm).

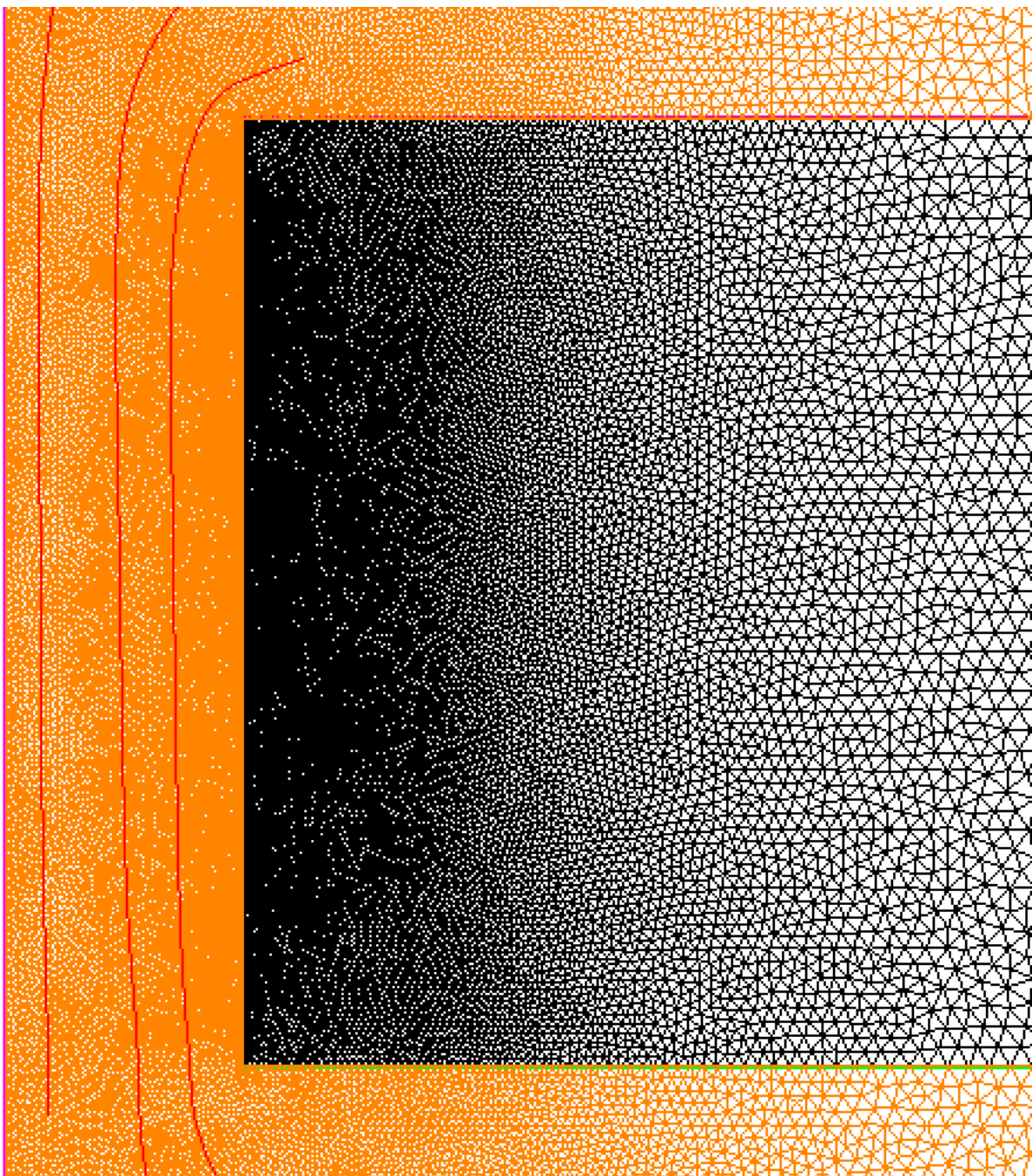


Fig. 5c – Three representative orbits for pore cylinder geometry.

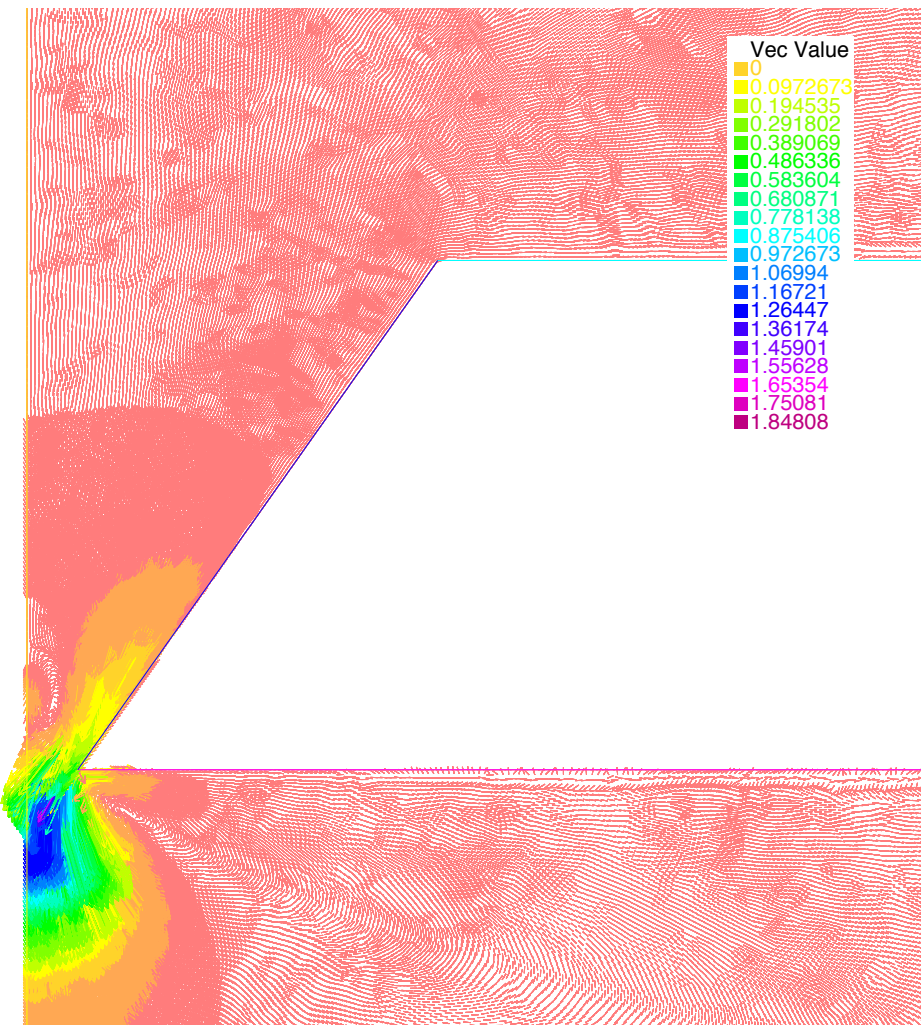


Fig. 6a – Scaled fluid velocity for inverted cone geometry, minimum radius 200 nm, depth 2 microns.

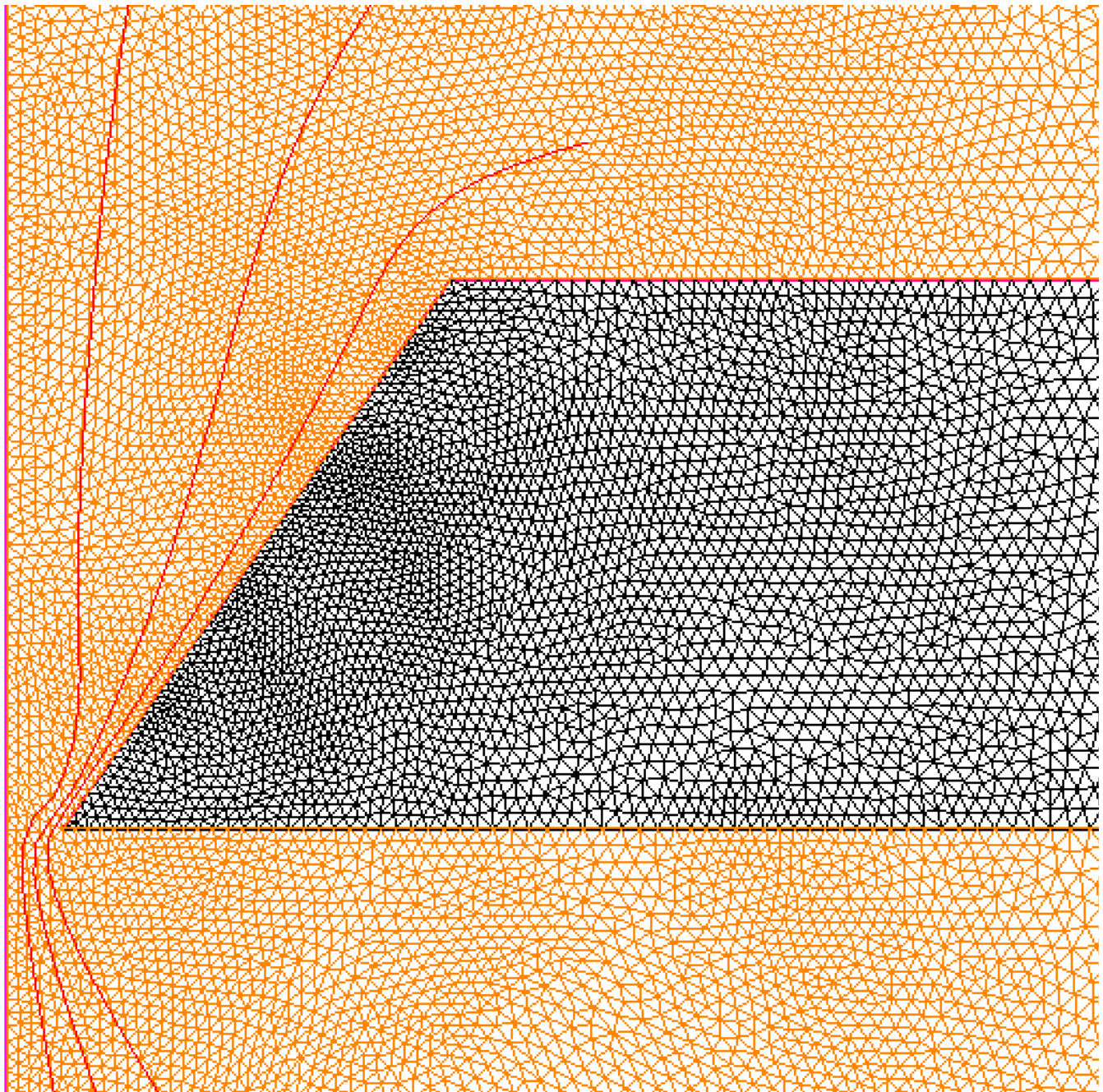


Fig. 6b – Three representative orbits for inverted cone, external field 10 V/mm.

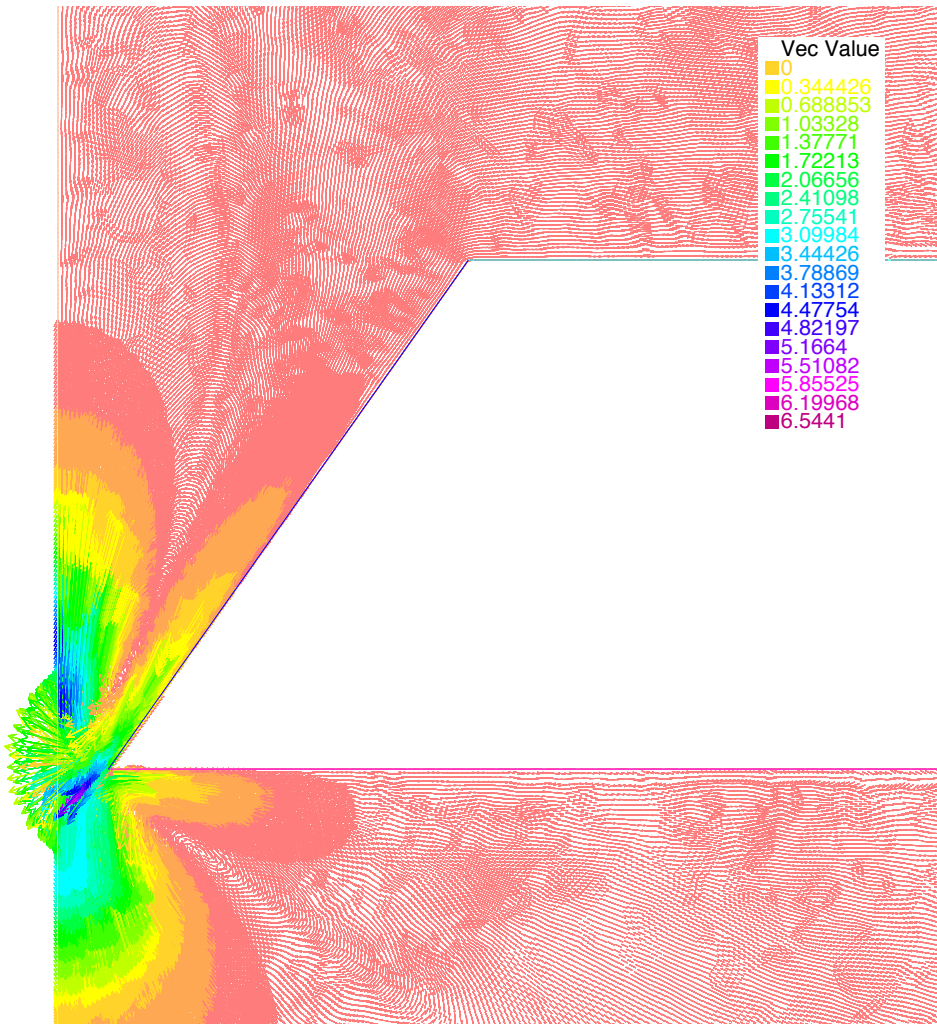


Fig. 7a – Scaled fluid velocity for inverted cone geometry, external field 20 V/mm.

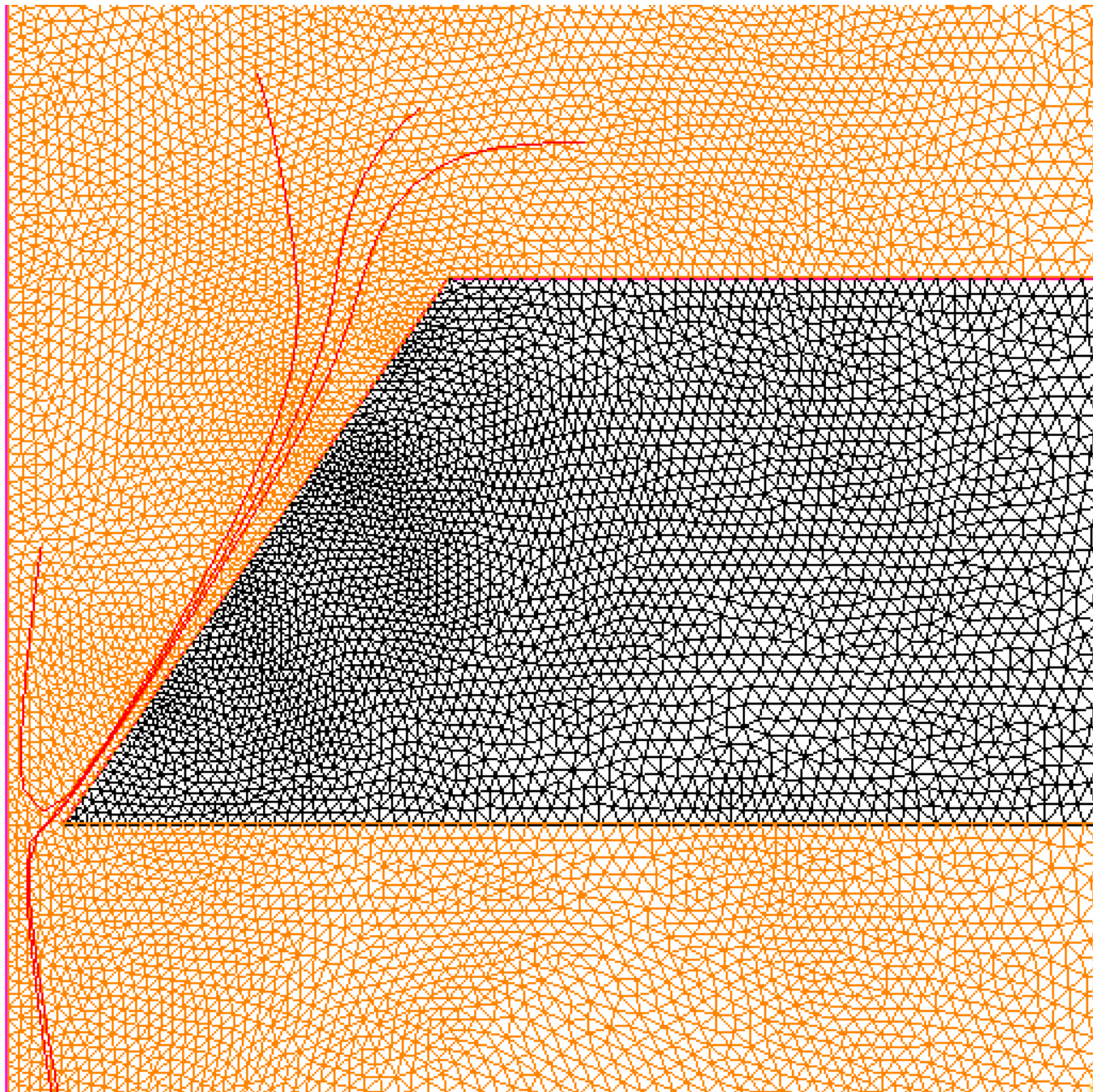


Fig. 7b – Three representative orbits for inverted cone, external field 20 V/mm. Note that the orbits for captured particles are close together near the surface and that particles starting nearer the pore axis do not exit the pore.

¹ Liu, Y., Sauer, J., Dutton, R. W., **Effect of electrodiffusion current flow on electrostatic screening in aqueous pores**, J. Appl. Phys., **103**, 084701 (2008), <http://dx.doi.org/10.1063/1.2906327> used a similar computational strategy.

² US patents 6413792, 7001792, inventors [Jon Robert Sauer](#), [Bart Jozef Van Zeghbroeck](#).

³ Kasianowicz, J. J., Brandin, E., Branton, D. & Deamer, D. W., **Characterization of individual polynucleotide molecules using a membrane channel**, Proc. Natl Acad. Sci. **93**, pp. 13770–13773 (1996).

This is the pioneering experimental report of electronic detection of a DNA molecule passing through a nanopore (α -haemolysin).

⁴ Deamer, D. W., Akeson, M., **Nanopores and nucleic acids: prospects for ultrarapid sequencing**, Trends Biotechnol., **18**, pp. 147–151 (2000).

⁵ Storm, A. J., Chen, J. H., Ling, X. S., Zandbergen, H. W., Dekker, C., **Fabrication of solid-state nanopores with single-nanometre precision**, Nat Mater, **2**, pp. 537–540 (2003).

⁶ Acharya, S., Edwards, S., & Schmidt, J., **Research highlights: nanopore protein detection and analysis**, Lab Chip, 2015, **15**, pp. 3424–3427 (2015), DOI: 10.1039/c5lc90076j.

⁷ National Science Foundation, CHAPS: Charge-Assisted Protein Sensing,
http://www.nsf.gov/awardsearch/showAward?AWD_ID=1159824&HistoricalAwards=false.

⁸ Hecht, F., **New development in FreeFem++**, J. Numer. Math., **20**, no. 3-4 (2012), pp. 251–265, and
<http://www.freefem.org/ff++/>.

⁹ <https://github.com/medilytix>.

¹⁰ Squires, T. M., Bazant, M. Z., **Induced-charge electro-osmosis**, J. Fluid Mech., **509**, pp. 217–252 (2004).

¹¹ https://en.wikipedia.org/wiki/Oseen_equations.

¹² Kirby, B. J., Hasselbrink Jr, E. F., **Zeta potential of microfluidic substrates: 1. Theory, experimental techniques, and effects on separations**, Electrophoresis, **25**, pp 187–202 (2004), Fig. 6. With $pC=3$.

¹³ See Deparis, S., **Numerical Analysis of Axisymmetric Flows and Methods for Fluid-Structure Interaction**

Arising in Blood Flow Simulation, École Poly. Lausanne, Thesis no. 2965 (2004), pp. 14,

http://sma.epfl.ch/~deparis/publications/PhD_thesis.pdf for the Stokes terms, especially those relating to the axisymmetric coordinate system.